The Impact of Non-Idealities on Low Power Magnetic Nozzle Thrust Performance

Timothy A. Collard* and Benjamin A. Jorns†
University of Michigan, Ann Arbor, MI, 48109, USA

The impact of non-ideal neutral pressure and plasma density distribution on the performance of a micro magnetic nozzle are investigated. These effects are believed to reduce performance. A quasi-1D model [1] is adapted to include these non-ideal effects. Plasma diagnostics, including a planar double Langmuir probe, Stabil ion gauge, and Laser Induced Fluorescence are used inform this model. It is experimentally determined that pressure effects become important when the Hall parameter due to electron-neutral collisions is low ($\Omega < 200$). Inclusion of pressure effects in the performance prediction model results in thrust and efficiency loss at high pressures or low magnetic nozzle strengths. The performance loss is due to changes in the the magnetic nozzle length and the location of the nozzle throat, and enhanced radial power losses. A ring discharge-like structure is observed when a magnetic nozzle employing a solenoidal antenna is experimentally interrogated, accompanied by a visible bright ring within the source tube and a corresponding off-axis peaked density profile. Using a transformation from cylindrical to magnetic coordinates for the magnetic nozzle expansion region of the quasi-1D models this off-axis peaked density profile slightly reduces the divergence efficiency of the nozzle. For the measured 390 G operating case the divergence efficiency of the nozzle was $\sim 2\%$ lower than if the device was operating with a center-peaked distribution, suggesting the divergence efficiency is relatively insensitive to plasma density profile shape. The elevated edge plasma densities associated with ring discharges enhance the power losses to the radial walls with the predicted radial losses of the 390 G case a factor of ~ 1.7 times the predicted losses of the lower magnetic field cases exhibiting weaker or no ring discharge structures. A discussion on the ramifications of these non-idealities on thruster design is included.

I. Nomenclature

β	=	Radial density average parameter, (-)
$\dot{m}$	=	mass flow rate, (kg/s)
ϵ_c	=	Collisional power loss, (eV)
ϵ_{e-}	=	Electron energy loss, (eV)
ϵ_{i-}	=	Ion kinetic energy at the sheath edges, (eV)
η_d	=	Divergence efficiency, (-)
η_m	=	Mass utilization efficiency, (-)
η_T	=	Total efficiency, (-)
η_{rf}	=	RF power coupling efficiency, (-)
Γ_0	=	Particle number flux, (/m^2-s)
$\langle v \rangle$	=	Average ion velocity, (m/s)
μ_0	=	Vacuum permeability, (H/m)
ν_{en}	=	Electron-neutral collision frequency, (1/s)
ψ	=	Magnetic nozzle streamline, (-)
ψ_v	=	Vacuum interface magnetic nozzle streamline (-)
ρ	=	Radial distance normalized by the source tube radius, (-)
ξ	=	Magnetic nozzle streamline normal, (-)
A	=	Nozzle cross-sectional area at the detachment point, (m^2)
A_0	=	Nozzle cross-sectional area at the detachment point, (m^2)

*Ph.D. Candidate, Department of Aerospace Engineering, University of Michigan, and AIAA Student Member.
†Assistant Professor, Department of Aerospace Engineering, University of Michigan, and Senior AIAA Member.

a_m = Magnet radius, (m)
B_r = Radial component of the magnetic field, (T)
B_z = Axial component of the magnetic field, (T)
F_0 = Upstream thrust, (N)
F_g = Thrust due to cold gas expansion, (N)
F_p = Thrust due to plasma expansion through the nozzle, (N)
F_T = Total thrust, (N)
h_R = Sheath edge-to-center density ratio, (-)
I = Current through the loop to generate the magnetic field, (A)
K_{exc} = Excitation rate constant, (m^{-3}/s
K_{iz} = Ionization rate constant, (m^{-3}/s
L_s = Source tube length, (m)
m_e = Electron mass, (kg)
m_i = Ion mass, (kg)
M_{det} = Detachment ion Mach number, (-)
n = Plasma number density, (m^{-3})
n_0 = Plasma number density at the throat, (m^{-3})
P_{abs} = Absorbed power, (W)
P_T = Total power, (W)
p_T = Total momentum, (kg-m/s)
p_z = Axial momentum, (kg-m/s)
q = Fundamental charge, (C)
r = Radial position, (m)
R_s = Source tube radius, (m)
r_{tp} = Radial position of the turning point of the bounding field line, (m)
T_e = Electron temperature, (eV)
T_g = Neutral particle temperature, (eV)
u_B = Bohm velocity, (m/s)
v_g = Neutral gas velocity, (m/s)
z = Axial position, (m)

II. Introduction

Propulsive magnetic nozzles are a form of electric propulsion where thrust is generated by converting thermal energy into directed kinetic energy via a convergent-divergent nozzle [2–16]. The converging-diverging magnetic nozzle topography is imposed by an external series of permanent magnets or electromagnets. The nozzle is generally contoured to confine the plasma within the source region and limit radial diffusion to the walls. The plasma is created by injecting neutral propellant into the ionization region where radio frequency (RF) or microwave power is coupled into the electrons via an antenna. The plasma then expands and accelerates through the converging-diverging magnetic nozzle section. Thrust is generated by the plasma expansion process via diamagnetic currents within the plasma and interaction with the magnetic circuit. Net thrust is only produced if the plasma detaches from the closed magnetic nozzle field lines downstream. Figure 1 illustrates this generalized process.

Magnetic nozzles possess several advantages as thrusters, including theoretical long lifetime due to the absence of a plasma-wetted electrode which also allows the use of a wide range of propellants. These characteristics can be attractive for long duration missions and missions requiring in-situ refueling, such as mining operations and multi-destination exploratory missions. However, these types of missions are currently not feasible due to the performance of state-of-the-art magnetic nozzles achieving total efficiencies of ~ 8% at ~ 2 kW [3]. This does not compare favorably to the ~ 60% efficient Hall Effect Thrusters [17] operating at a similar power level.

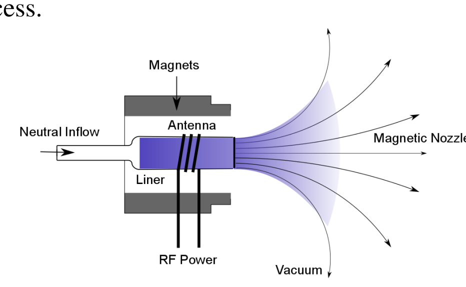

Fig. 1 A generalized propulsive magnetic nozzle configuration.

To explain this performance deficit several magnetic nozzle performance models have been proposed [1, 10, 18] for low to moderate power levels and small to moderate thruster sizes, but these models do not include non-idealities in the performance predictions. Within the context of these ideal models the low performance is generally attibuted to radial wall losses within the source tube and low overall electron temperatures. However, in the literature the community has observed additional non-ideal phenomena that impact thrust performance across a range of thruster configurations and operating conditions. These phenomena include hot electron and high density populations confined to the edges of the nozzle [16], near-field resistive detachment [19], and a reduction in nozzle efficiency with increasing background pressure [20]. The following questions then arise: *1) how do these non-idealities, such as off-axis density concentrations and pressure effects, impact thrust performance? and 2) could the presence of these non-ideal effects further explain the performance trends measured for these devices in ground testing facilities?* To answer these questions we couple experimental measurements with adaptations of the existing models to determine if these phenomena degrade thrust performance.

In this work we use a suite of plasma diagnostics to measure the plasma and neutral properties within the plume of a flexible magnetic nozzle testbed source to inform the adapted performance models and to determine the threshold when pressure effects begin to impact the expanding nozzle region. A summary of the existing quasi-1D model and the proposed adaptation to extract divergence efficiency is outlined in Section III. Section IV details the experimental apparatus. The results of the experiments are presented in Section V and the corresponding impact of density profile shape and pressure effects are discussed in Section VI.

III. Theoretical Model

In order to predict the thrust performance of magnetic nozzles operating in a range of operating conditions and with varying architectures Lafleur [1] has proposed a generalized quasi-1D model. For completeness and to facilitate the discussion of the changes proposed in this paper a brief overview of the model is included in the Appendix and the key modifications are discussed in this section.

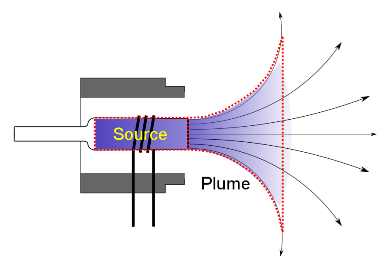

Fig. 2 A reference magnetic nozzle that is split into the two control volumes used in the model.

At a high level, the model splits a generalized RF magnetic nozzle into two sections, as shown in Figure 2: the source tube region where RF power is coupled to free electrons that then collide with neutral propellant creating ions through impact ionization, and the plume expansion region where the thermal energy of the plasma is converted into directed kinetic energy via a convergent-divergent magnetic nozzle. The ionization region is defined as the control volume bounded by the walls of the source tube and extending to the nozzle throat. At the throat the ions are assumed to achieve sonic velocities. The expansion region is then defined as the control volume extending from the nozzle throat to the plasma detachment location and bounded by the magnetic field that grazes the wall at the exit plane of the source tube.

The detachment location is where the plasma streamlines no longer coincide with the diverging magnetic nozzle streamlines. The precise definition of the detachment location is a current topic of discussion and a self consistent and experimentally validated description has not yet been determined. Some of the proposed criteria are when the ion Larmor radius exceeds the nozzle throat radius [1], when the ion streamlines separate from the magnetic field lines by 4% [8], plasma demagnetization based on the relative magnitude of the local particle gyroradii and the plasma gradient length scale [11], and electrostatic separation where the massive unmagnetized ions do not diverge at the same rate as the magnetized electrons in the highly divergent portion of the nozzle [9, 11, 21]. For purposes of closing the model the criterion used herein is that detachment occurs at the magnetic nozzle turning point as proposed by Little [8] based on the electrostatic separation work by Merino and Ahedo [9], unless otherwise noted. Beyond this turning point minimal momentum is transferred to the thruster so detachment can be assumed. The turning point can be determined iteratively from the exact cylindrical solution for the magnetic field topography generated by a single current loop [22] and by solving for $B_z = 0$, where

$$B_r = \frac{\mu_0 I z}{2\pi\alpha_m^2\beta_m r}\left[(a_m^2 + r^2 + z^2)E(k^2) - \alpha_m^2 K(k^2)\right], \tag{1}$$

$$B_z = \frac{\mu_0 I}{2\pi\alpha_m^2\beta_m}\left[(a_m^2 - r^2 - z^2)E(k^2) + \alpha_m^2 K(k^2)\right], \tag{2}$$

$$\alpha_m^2 = a_m^2 + r^2 + z^2 - 2a_m r, \tag{3}$$

$$\beta_m^2 = a_m^2 + r^2 + z^2 + 2a_m r, \tag{4}$$

and

$$k^2 = 1 - \frac{\alpha_m^2}{\beta_m^2}. \tag{5}$$

In these expressions a_m is the current loop radius, I is the current flowing in the loop, and (r, z) is the location in cylindrical coordinates.

In the nozzle section, the thrust generated by the expansion of the plasma through the nozzle can be determined from combining the ion and electron momentum and continuity equations to yield

$$\frac{1}{2}(M_{det}^2 - 1) - ln(M_{det}) = ln\left(\frac{A}{A_0}\right), \tag{6}$$

which is a relationship between the area expansion ratio of the nozzle and the ion velocity. M_{det} is the ion Mach number at the detachment location, A is the cross sectional area of the nozzle at the detachment location, and A_0 is the throat area. For this relationship to hold the plasma within this expanding section is assumed to be collisionless, attached to the nozzle field lines up to the detachment point, and perfectly confined by the bounding magnetic field line.

This expression of thrust is only part of the important performance metrics; the other useful metric is thrust efficiency. To predict the thrust efficiency an estimate of the total power must be determine. The power absorbed by the plasma within the source tube is equal to the power loss at the boundaries,

$$P_{abs} = \frac{1}{2}\beta n_0 u_B A_0(\epsilon_c + \epsilon_{ic} + \epsilon_{ec}) + \frac{1}{2}\beta n_0 u_B A_0(\epsilon_c + \epsilon_{i0} + \epsilon_{e0}) + \frac{\pi q u_B R_s h_R n_0 L_s}{\gamma\xi} ln\left(\frac{1+\xi}{1-\xi}\right)(\epsilon_c + \epsilon_{ir} + \epsilon_r), \tag{7}$$

where the first term represents the power lost at the back wall, the second term is the power lost at the exit plane, and the last term is the radial power lost. The energy loss terms are defined as

$$\epsilon_c = \epsilon_{ion} + \frac{K_{exc}}{K_{iz}}\epsilon_{exc}, \tag{8}$$

$$\epsilon_{ec} = \epsilon_{er} = 2T_e + \frac{T_e}{2} ln\left(\frac{m_i}{2\pi m_e}\right), \tag{9}$$

$$\epsilon_{e0} = \frac{1}{2}M_{det}^2 T_e + 2T_e, \tag{10}$$

and

$$\epsilon_{ic} = \epsilon_{i0} = \epsilon_{ir} = \frac{T_e}{2}, \tag{11}$$

and capture losses due to collisions, the sheath inside the source, and electron transport at the boundaries of the source region. In these equations β is the average density coefficient, n_0 is the plasma density in the source region, u_B is the Bohm velocity, h_R is the sheath edge-to-center density ratio, L_s is the source tube length, R_s is the source tube radius, ϵ_{ion} is the ionization energy threshold for the species, ϵ_{exc} is the excitation energy threshold, K_{iz} is the ionization rate, K_{exc} is the excitation rate, T_e is the electron temperature, m_i is the ion mass, and m_e is the electron mass. γ and ξ are defined by Eqs. 22 and 23 in the Appendix.

The total efficiency can be estimated by

$$\eta_T = \frac{F_T^2}{2\dot{m}P_T} \tag{12}$$

where $P_T = P_{abs}/\eta_{rf}$, which incorporates the efficiency of RF power coupling into the plasma within the source region. In this expression F_T is the total thrust, $\dot{m}$ is the propellant mass flow rate, P_{abs} is the absorbed power, and η_{rf} is the RF power coupling efficiency. However, this form of the total efficiency does not readily reveal a key source of efficiency reduction: the divergence efficiency, or the ratio of axial momentum to total momentum.

In the base cylindrical quasi-1D model by Lafleur [1] it is difficult to track the momentum vectors throughout the nozzle section, and therefore to determine the divergence efficiency. However, modification of the model leveraging the assumptions of a collisionless plume and perfect attachment to the nozzle streamlines up to the detachment point allows the nozzle section to be transformed into magnetic coordinates - the local coordinate vectors are parallel ($\hat{\psi}$) and perpendicular ($\hat{\xi}$) to the magnetic streamlines - while retaining the advantages of a quasi-1D model. The first term in the Taylor expansions of Eqs. 1 and 2 and the appropriate derivatives to determine the streamfunction yields the (r, z) to (ψ, ξ) transformation:

$$\psi = \frac{(r/a_m)^2/2}{[1 + (r/a_m)^2 + (z/a_m)^2]^{3/2}} \tag{13}$$

and

$$\xi = \frac{(z/a_m)/2}{\left[(r/a_m)^2 + (z/a_m)^2\right]^{3/2}}, \tag{14}$$

where $\xi(r, z)$ holds for $(z/a_m) > 1$.

At the nozzle throat the streamlines are parallel to $\hat{z}$ allowing for a simple coordinate transformation of the empirical density profiles used in the model from $n(r)$ to $n(\psi)$. Due to the original model assumptions of self-similarity and perfect attachment to the nozzle streamlines the $n(\psi)$ profile is valid up to the detachment point and the local velocity vector is tangent to the nozzle streamlines. This allows the total momentum to be defined as

$$p_T = 2\pi \int_0^{\psi_v} n(\psi)\langle v\rangle r d\psi \tag{15}$$

and the axial momentum as

$$p_z = 2\pi \int_0^{\psi_v} n(\psi)\langle v\rangle_z r d\psi, \tag{16}$$

where $\langle v\rangle$ is the average velocity determined from the quasi-1D analysis and ψ_v is the vacuum-interface streamline that grazes the source tube wall. The divergence efficiency is then

$$\eta_d = \frac{p_z^2}{p_T^2}. \tag{17}$$

This analysis provides insight into the effect of plume divergence on thrust efficiency. In many cases this model may yield a more accurate efficiency prediction than a traditional cylindrical quasi-1D model because it includes more radial information and does not rely solely on the average of the density across an area-slice of the nozzle. Based on Eqs. 15 and 16 the shape of the density profile impacts the efficiency performance; if the density is concentrated off centerline a greater portion of the velocity is directed radially due to the higher divergence of the nozzle streamlines away from centerline. For thruster architectures that generate discharges with off-center or only moderately centerline-peaked density concentrations the performance impact can be predicted and the viability of the architecture assessed.

In addition to power coupling structures within the source tube another set of non-idealities arises from pressure effects, including elevated background pressure and the presence of a high neutral pressure exiting the source tube without being ionized. It has previously been asserted [19] that the presence of a neutral population can impact the nozzle confinement and expansion processes by enhancing cross field transport through electron-neutral collisions. The onset of the breakdown of confinement could be predicted by the Hall parameter, defined as

$$\Omega = \frac{qB}{m_e \nu_{en}}, \tag{18}$$

where B is the local magnetic field strength and ν_{en} is the electron-neutral collision frequency. When $\Omega \gg 1$ the nozzle confines the plasma and guides the expansion process. If this inequality is not satisfied the nozzle does not confine the plasma. If the inequality is not satisfied in the far-field, possibly due to high background pressure, then the nozzle is effectively shortened and the plasma is prematurely detached before reaching the nozzle turning point. This leads to a reduction in the detachment ion Mach number via Eq. 6 and a corresponding reduction in thrust and total efficiency through Eqs. 12 and 26. Similarly, if the propellant is not sufficiently ionized within the source tube, resulting in a largely neutral exhaust, the throat can be shifted downstream due to the enhanced electron-neutral collision frequency that can drive $\Omega \ll 1$. If the plasma reattaches to the magnetic nozzle downstream due to the gradient length scale of the neutral density exceeding the gradient length scale of the magnetic nozzle the throat area is much larger than the nominal throat within the source tube, resulting in a reduced ion Mach number when the particles detach in the far-field. Additionally, there is an extended loss region in the near-field when the plasma is not confined by the magnetic nozzle, which also reduces the total thrust and efficiency. By calculating the Hall parameter throughout the plume we can incorporate these non-ideal effects into the performance predictions.

IV. Experimental Setup

In this section the experimental apparatus used to investigate the non-idealities outlined in Section III is described. The Magnetic Detachment eXperiment (MDX) [19] is summarized and the diagnostics used to make the measurements that inform the model results in Section V are outlined.

A. The Magnetic Detachment eXperiment

The MDX is a flexible testbed magnetic nozzle source ~ 13 cm in diameter with the capability of integrating plasma source tubes up to 3 cm in diameter. The converging-diverging magnetic nozzle section is generated by a solenoid constructed of enamel-coated copper magnet wire and driven by an external DC laboratory power supply. The electromagnet is capable of producing peak axial magnetic fields of up to ~ 900 G. An external radio frequency (RF) power supply generates power that is then matched to the antenna-plasma load and is coupled to the plasma via a hollow copper inductive antenna. The electromagnet and antenna are open-loop water cooled to maintain steady-state operating temperatures below the 240 °C rating of the magnet wire. An external xenon reservoir supplies propellant to the MDX. To minimize stray RF the MDX is enclosed within a Faraday mesh, with openings for connections and the plasma expanding through the magnetic nozzle. Figure 3 is a photo of the MDX mounted in the test configuration.

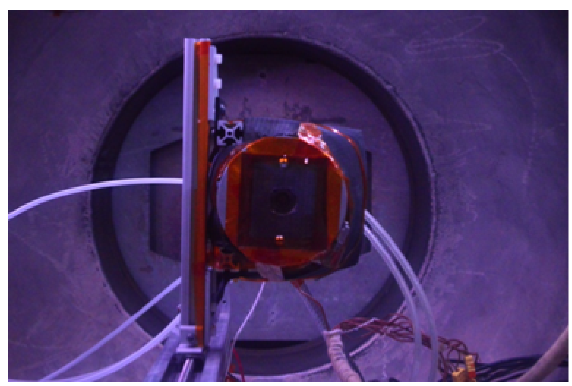

Fig. 3 A photograph of the MDX installed in the Junior Test Facility.

B. Vacuum Facility

The experiments were conducted in the Junior Test Facility connected to the Large Vacuum Test Facility at the University of Michigan. Junior is a 3 meter long by 1 meter diameter stainless steel clad vacuum chamber backed by a turbopump and a cryo pump, nominally rated at 38,000 L/s on xenon. The effective pumping speed for the experiments described in this paper was ~ 15,000 L/s on xenon. With this pumping capacity Junior is capable of achieving base pressures of ~ 1×10^{-8} Torr and a background pressure of ~ 4×10^{-5} Torr during the MDX operation at neutral flow rates up to 3 mg/s.

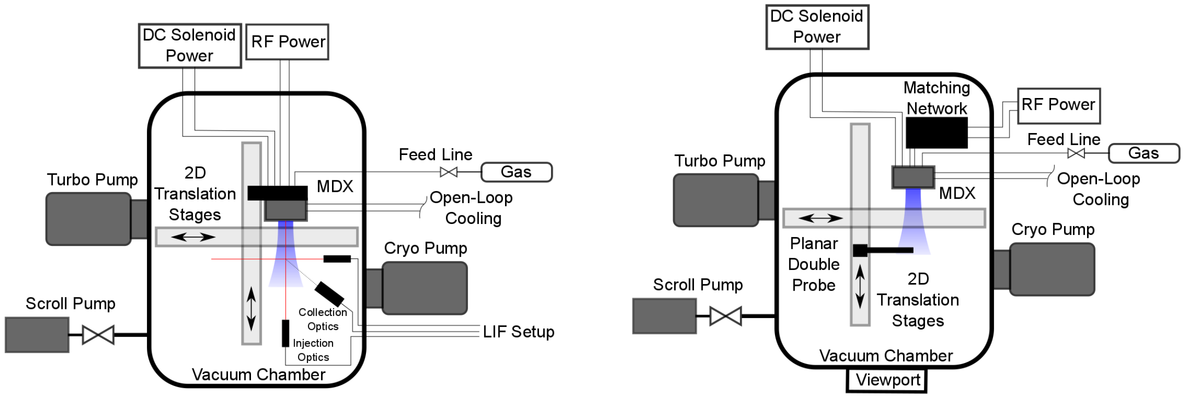

(a) (b)

Fig. 4 (a) The experimental setup used to measure the ion streamlines relative to the magnetic nozzle streamlines. Note that for this setup the RF matching network is located outside of the vacuum chamber. (b) The experimental setup used to measure the exit plane density profile of the MDX while operating in the ring discharge modes.

C. Diagnostics
To answer the question *how do non-idealities affect magnetic nozzle performance?* plasma measurements within the plume and at the source exit plane are required, including spatial neutral density, magnetic field, plasma density, and ion velocity profiles. These properties were mapped with a combination of probe diagnostics, including a planar double Langmuir probe and a Pitot probe, and a 2D time-averaged Laser Induced Fluorescence (LIF) setup [23]. To accommodate the small size of the MDX the planar double Langmuir probe was constructed of two 0.25 mm diameter tungsten rods housed within a 1/16" diameter double-bore alumina tube. The LIF was used to measure the axial and radial ion velocity distributions in the plume near-field. To preserve alignment the MDX was moved using a pair of linear translation stages while the LIF injection and collection optics remained fixed thereby allowing the 1 mm diameter LIF measurement spot to interrogate different locations within the plume. This LIF setup is illustrated in Figure 4(a). For the invasive diagnostics the experimental setup was modified and the MDX was fixed relative to the planar double Langmuir probe that was mounted on the linear stages. An MKS 370 Stabil ion gauge, mounted in place of the double probe in Figure 4b, was used to measure the spatial variations in the neutral pressure distribution of the MDX while flowing 3 mg/s of xenon. The Stabil gauge setup included an integrated 1/8" diameter pitot tube with a 90° bend. The magnetic nozzle topography at various electromagnet setpoints was measured in atmosphere using a 3-axis Gaussmeter with a resolution of 0.01 G in each measurement.

V. Results
In this section experimental plasma measurements of the density distribution at the exit plane of the MDX, the ion velocity vectors in the near-field plume, and the spatial map of the neutral density within the plume are presented. These quantitative results are supplemented by qualitative photos and light intensity profiles of the MDX to help define the ring discharge mode. The quantitative results are also used to inform the performance prediction model that includes non-ideal nozzle effects and the results of the model are presented.

A. Qualitative Ring Discharge Results
When the MDX was operated with a multi-turn solenoidal antenna the plasma discharge shifted from a dull, pink color indicative of a primarily capacitive xenon mode to a bright, white/blue discharge indicative of a primarily inductive mode. At this transition point the tune on the matching network significantly shifted and the reflected power generally dropped from ~ 50 W to ~ 25 W while the forward power remained set at ~ 175 W. Upon further investigation at this steady state operating power and a flow rate of 0.5 mg/s of xenon the visible structure within the source region changed as the magnetic nozzle strength was increased. Typically, for xenon the light spectrum visible to the human eye is

(a)

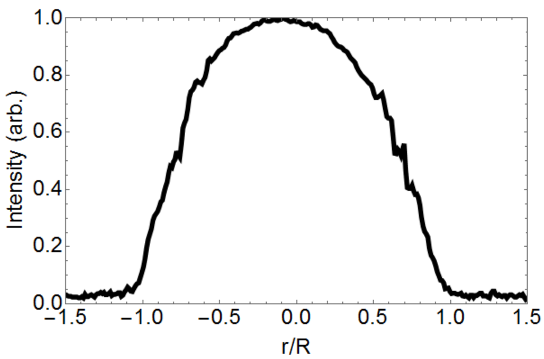

(b)

Fig. 5 (a) A photograph of MDX operating at ∼ 150 W, 0.5 mg/s of xenon, and a magnetic nozzle throat strength of 39 G. (b) The corresponding intensity of the visible spectrum axial light intensity of the discharge.

(a)

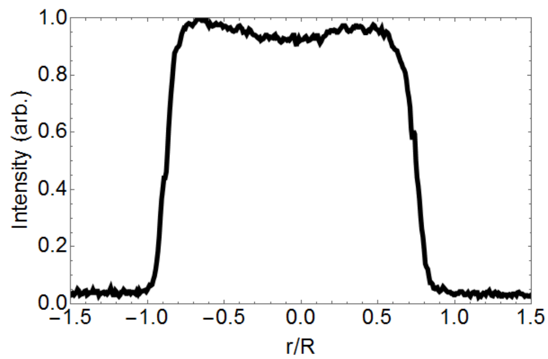

(b)

Fig. 6 (a) A photograph of MDX operating at ∼ 150 W, 0.5 mg/s of xenon, and a magnetic nozzle throat strength of 98 G. (b) The corresponding intensity of the visible spectrum axial light intensity of the discharge.

(a)

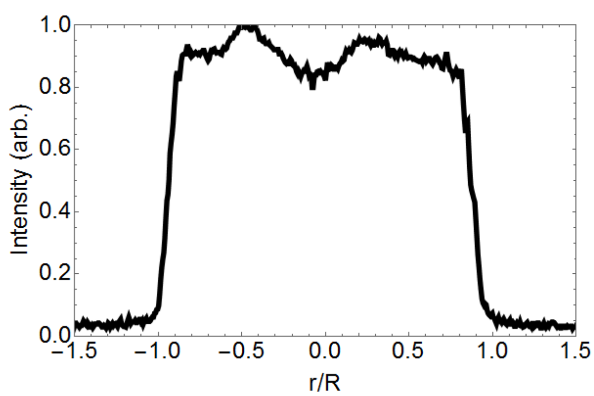

(b)

Fig. 7 (a) A photograph of MDX operating at ∼ 150 W, 0.5 mg/s of xenon, and a magnetic nozzle throat strength of 390 G. (b) The corresponding intensity of the visible spectrum axial light intensity of the discharge.

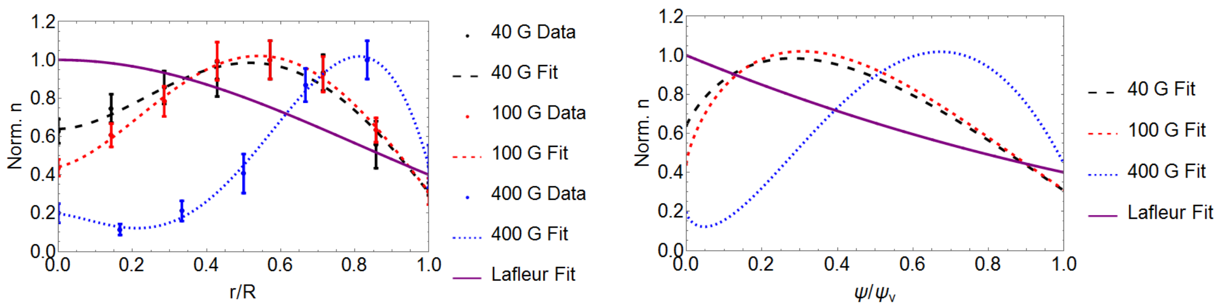

(a) (b)

Fig. 8 (a) The plasma density profile measured in the MDX operating at at $\sim$ 150 W, 0.5 mg/s of xenon, and various magnetic nozzle throat strengths, and the associated profile fits. The density profile fit used by Lafleur [1] in the initial quasi-1D performance model is also included. The profile is based on fits of published experimental magnetic nozzle data. Note that the errorbars are estimated using resampling of the I-V double probe traces. b) The plasma density profiles transformed into the ψ-ξ magnetic coordinates.

comprised of primarily excited neutral lines and a few ion lines [24]. However, assuming a moderately uniform neutral density within the source tube the light intensity could be correlated to the local power deposition because the region of maximum power deposition would result in a higher fraction of electrons exceeding the minimum energy threshold for excitation collisions. At very low magnetic fields the highest light intensity was peaked at the centerline, as shown in Figure 5 for the 39 G case. As the magnetic field strength was increased the peak light intensity shifted radially toward the walls of the source tube and an intensity deficit began to appear on centerline, as illustrated by the 98 G and 390 G cases in Figures 6 and 7, respectively. These qualitative results are consistent with the description of ring discharges in inductively coupled plasmas (ICPs) found within the literature [25–27].

B. Centerline Density Deficit due to the Ring Discharge Structure

While the qualitative results discussed in the previous section are promising, they do not confirm that the structure is a ring discharge. As noted by Kinder and Kushner [25] in their work modeling magnetically enhanced inductively coupled plasmas (MEICPs), above a critical magnetic field strength within the ionization region the peak power deposition zone shifted radially outward. In these cases the density profile also exhibited an off-center peak coinciding with the zone of maximum power deposition. While the exact magnetic field threshold is dictated by the antenna geometry, the source size, the propellant species, and the neutral pressure within the ionization region the critical threshold identified by Kinder and Kushner [25] was 150 G for a MEICP operating at 1 kW on argon, putting this type of discharge within the operating range of many propulsive magnetic nozzles [3, 8].

A key piece of evidence supporting the theory that the MDX is operating in a ring discharge mode is the presence of a density dip on source centerline that is dependent on the magnetic field strength. For reference, the center-peaked density profile used in the Lafleur [1] model is shown in Figure 8(a) - this profile does not exhibit behavior consistent with a ring discharge. Shifting to the MDX, Figure 8(a) shows the plasma density profile at the source exit plane at several magnetic nozzle operating conditions. In the weak magnetic field case corresponding to a throat strength of 39 G there appears to be a slight plasma density dip on centerline. As the magnetic field is increased to 98 G the centerline density trough becomes more pronounced. In the highest magnetic field case of 390 G the plasma density is small on centerline and heavily peaked near the wall. These plasma density results appear to indicate the presence of a ring discharge structure within the source region and are consistent with both the qualitative results in the previous section and the results of Kinder and Kushner [25].

C. Measured Hall Parameter and Ion Velocities

Another set of non-idealities can be caused by pressure effects interacting with the magnetic nozzle, primarily through enhanced cross-field transport or by causing premature detachment. To calculate the performance impact of these two effects a criterion for significant pressure relative to the local magnetic nozzle strength must be determined. Experimentally, three quantities are required to determine this criterion; the neutral pressure distribution throughout the plume, the magnetic field topography of the magnetic nozzle, and the ion velocity vectors.

The magnetic topography was previously spatially mapped over a 40×30 cm grid with 5 mm spatial resolution

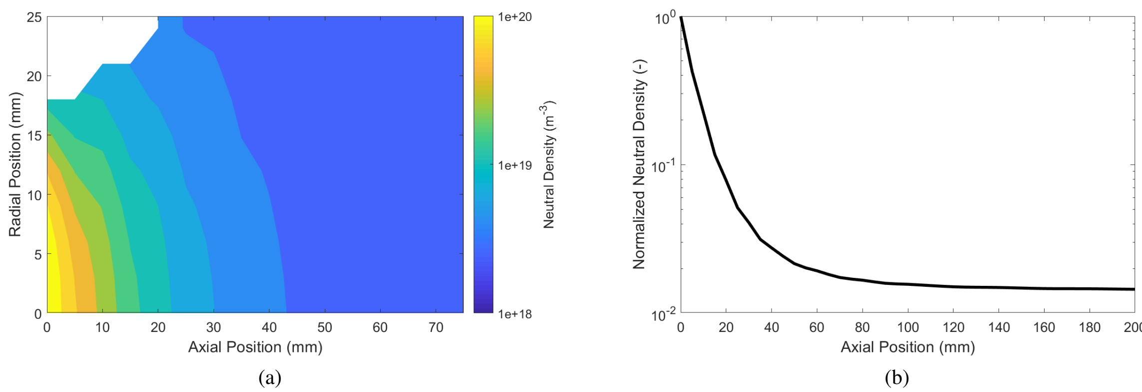

Fig. 9 (a) A 2D map of the neutral density extracted from measurements of the neutral pressure made with a Stabil ion gauge equipped with a pitot tube. (b) The normalized neutral pressure on centerline.

using a 3-axis Gaussmeter for electromagnet peak field strengths ranging from 98 G to 584 G [19]. The neutral pressure within the plume was mapped using a Stabil ion gauge with a pitot probe attachment. The Stabil grid was dictated by the most divergent magnetic field case. Figure 9 shows the spatial neutral density map and centerline map of the MDX with a propellant flow rate of 3 mg/s of xenon. Note that the neutral measurements were taken without plasma.

The ion velocity vectors were determined using radial and axial LIF data. The mean axial and radial velocities were determined by taking the moment of the sums-of-Gaussian fits to the raw LIF data. Like the Stabil grid, the LIF grid limits were dictated by the most divergent magnetic field case and the deteriorating signal-to-noise ratio of the LIF signal as the plasma density decreased downstream of the exit plane. As depicted in Figure 10 for all cases the near-field ions expanded isotropically and then started to bend as the Hall parameter reached a critical threshold of ~ 200. As the magnetic field increased this threshold was exceeded closer to the source exit plane, suggesting that the nozzle begins closer to the exit plane. If the magnetic nozzle strength is sufficiently high or the un-ionized neutral propellant flow is sufficiently low the plasma is attached throughout the nozzle.

VI. Discussion

These experimental results can be used to seed the performance models which can be used to determine the impact of density profile and neutral pressure non-idealities on thruster performance. This section will explore the performance impact of these non-idealities and comment on the design ramifications.

A. Efficiency Impact of Ring Discharges

A natural consequence of the presence of an off-axis density peak within the source region is a reduction in the divergence efficiency of the magnetic nozzle, assuming that the nozzle is collisionless and the plasma is attached to the field lines. In a converging-diverging magnetic nozzle the field lines originating near the edges of the source tube diverge more than the lines near the center; in the presence of a ring discharge a higher fraction of the plasma is confined to the highly divergent field lines near the edge of the nozzle resulting in a larger radial component of the ion velocity at the detachment location. Since the desired thrust vector is axial this phenomenon degrades the efficiency of the nozzle. The severity of this performance degrading effect can be examined by transforming the magnetic nozzle section of the model into the (ψ, ξ) magnetic coordinates and calculating the divergence efficiency using Eq. 17, assuming a detachment location prescribed by Little's 4% plasma streamline deviation from the nozzle lines [8]. For reference, the transformation of the density profiles into $n(\psi)$ are shown for each non-trivial case in Figure 8.

To investigate the sensitivity of the divergence efficiency to plasma density profile we can examine the worst case MDX operating condition - the 390 G ring discharge case. This is the worst case because the relatively high magnetic field results in an increase in the nozzle length, thereby increasing the divergence of the edge magnetic nozzle field lines. It also exhibits the most pronounced ring discharge density profile with the highest edge density. Using the measured ring discharge plasma density profile and the MDX dimensions the divergence efficiency is estimated to be $\sim 25\%$. For

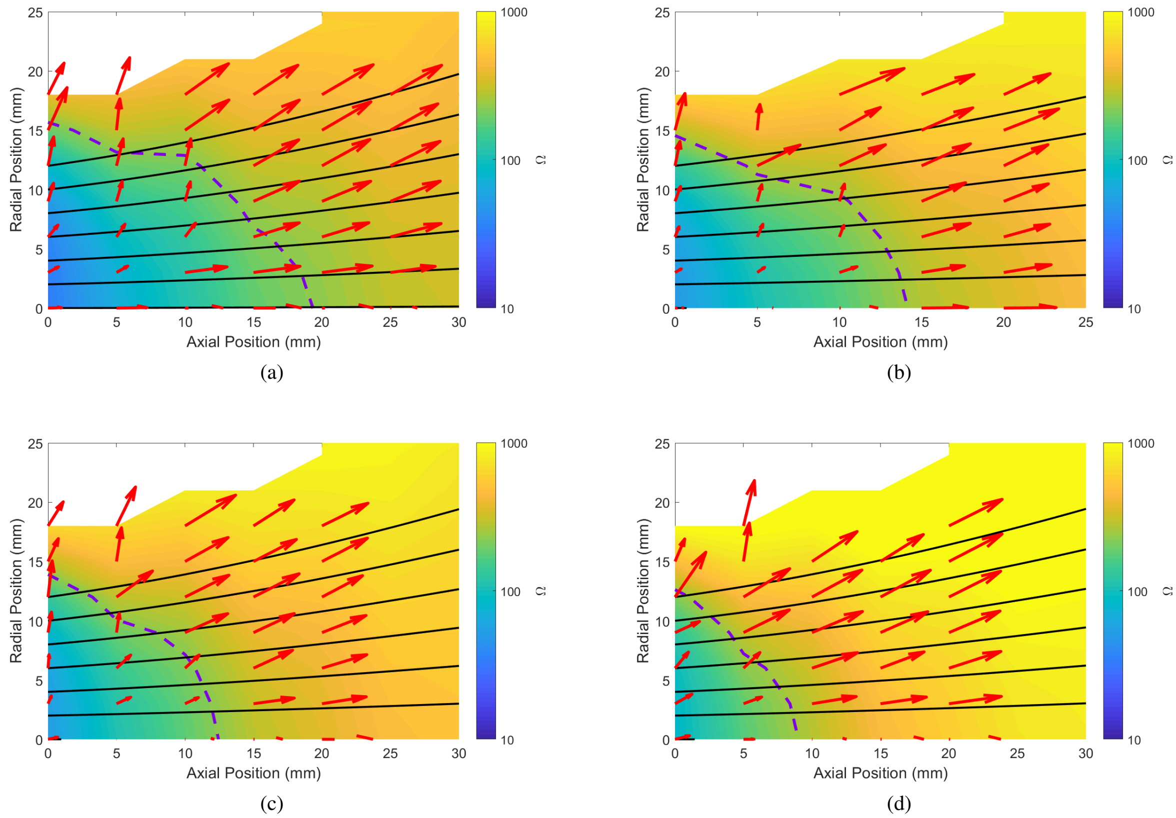

Fig. 10 An overlay of the magnetic nozzle streamlines, the Hall parameter, and the local ion velocity vectors measured by LIF for the MDX operating at ~ 150 W, 3 mg/s of xenon, and a magnetic nozzle throat strength of (a) 200 G, (b) 300 G, (c) 400 G, and (d) 500 G. Note that the ion velocity vectors start bending at $\Omega \sim 200$, as denoted by the dashed contour line on each figure.

comparison, if the plasma density profile matched the center-peaked Lafleur profile [1] the divergence efficiency is estimated to be $\sim 27\%$. This minimal reduction in divergence efficiency due to the presence of a ring discharge structure suggests that this efficiency performance is relatively insensitive to plasma density profile shape within the operating envelope of the MDX. At higher magnetic field strengths or larger thruster diameters the presence of this structure may exert a slightly greater influence on the divergence efficiency as the edge density increases, but this is likely to remain a small effect in the context of micropropulsion thruster architectures.

The presence of a ring discharge structure, and the associated high plasma density near the source tube walls, also impacts the power lost to the radial walls. As stated in Eq. 7 this power loss is affected by the plasma density at the wall, so an elevated edge plasma density increases the radial losses and decreases the power entering the nozzle assuming constant power operation. This results in an effective effiency degradation through the reduction of the fraction of power contributing to thrust compared to the total input power. As illustrated by Figure 11 the enhanced edge plasma density present in the 390 G ring discharge operating condition increases the power lost to the radial walls by a factor of ~ 1.7 compared to the other two ring discharge cases. The relatively high radial losses of the Lafleur profile [1] are due to the small size of the MDX source tube; the ion Larmor radius is on the order of the source tube radius so the sheath edge-to-center ratio is maximum at ~ 0.4. The sheath edge-to-center ratio decreases at higher magnetic nozzle strengths and with larger thruster diameters. Conversely, in a thruster architecture conducive to sustaining a ring discharge an increase in the magnetic field excacerbates this radial power loss rather than minimizing it via better confinement within the source region.

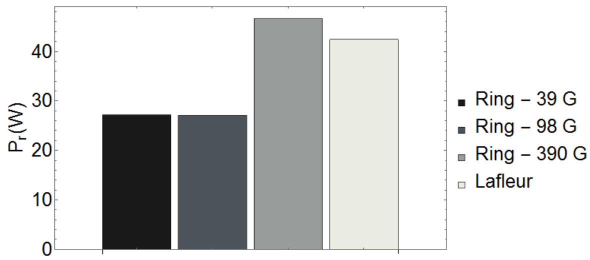

(a)

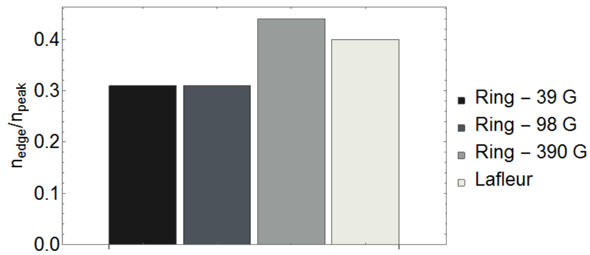

(b)

Fig. 11 (a) The estimated power lost to the radial walls of the MDX operating in the ring discharge conditions compared to the case where it operates with a density profile well modeled by the Lafleur fit [1]. (b) The corresponding density at the wall with respect to the maximum density within the profile.

B. Impact of Near-Field Resistive Detachment on Performance

The impact of near-field resistive detachment can be modeled by using the critical Hall parameter threshold of $\Omega = 200$ to determine if the plasma is detached in the near-field, and, if it is detached, where the plasma reattaches. For the MDX, with the electromagnet modeled as a single current loop and the throat density set to $\sim 2 \times 10^{17}$ m^{-3}, the impact of the neutral pressure exiting the source region is shown in Figure 12. As illustrated by Figure 12(a) the plume remains attached for all conditions until a neutral exhaust pressure of $\sim 1 \times 10^{-5}$ Torr is reached. Near-field detachment occurs at higher pressures for higher magnetic fields. The near-field detachment has two ramifications on performance: 1) the source region is lengthened and becomes $L_s = L_{s,a} + Z_{det}$, which results in larger radial losses and 2) the throat cross-sectional area is larger due to the divergence of the magnetic nozzle lines, which results in a net loss of thrust via Eqs. 6 and 26 due to the reduced plasma expansion from the new throat to the nozzle turning point. The enhanced radial power loss is shown in Figure 12(b) where, at high neutral exhaust pressures, the radial losses can be several times the losses of the case where the plume had remained attached to the nozzle throughout.

The area reduction is shown in Figure 12(c), where the low pressure asymptote is due to the MDX source tube diameter and the radius of the single current loop electromagnet model. The reduced expansion through the remainder of the magnetic nozzle is illustrated by the reduction in the far-field detachment Mach number observed in Figure 12(d). The resulting reduction in the thrust production from the nozzle expansion process is shown in Figure 12(e), with the corresponding reduction in the total efficiency shown in Figure 12. Note that both of these ratios are relative to the fully attached nozzle performance quantities. The relatively minor reduction in both quantities is due to the definition of far-field detachment; by using the nozzle turning point criterion the nozzle area is large. If detachment happens upstream of this point the severity of the near field detachment is enhanced. Overall, the performance degradation worsens with increasing un-ionized neutral density being exhausted by the source. At very high near-field neutral pressures the confinement of the plasma by the magnetic nozzle diminishes and the nozzle effectively disappears. To a degree the onset of near-field resistive detachment is delayed by increasing the strength of the magnetic nozzle, but at high magnetic fields comparable to ECR source configurations [20] this effect can occur at neutral pressures comparable to those required to maintain a steady plasma discharge. A more pertinent solution is to ensure good power coupling throughout the source tube region, thereby reducing the propellant flow rate required to maintain a steady discharge and directly reducing the un-ionized exhaust by generating a denser plasma.

To clarify the underlying effects of the un-ionized neutral propellant that can lead to near-field resistive detachment the thruster dimensions and operating conditions can be specified. The trends become clear, as shown in Figure 13, if we use the MDX physical dimensions, the throat magnetic field strength is 800 G, and the propellant flow rate is 0.5 mg/s of xenon. Note that the magnetic field is of sufficient strength that the ion Larmor radius in the source region is smaller than the source tube radius, so we use the original Lafleur [1] detachment criterion - where $r_{Li} = r_s$.

At low power the thrust and the specific impulse is low due to the low ion fraction. The relatively high total efficiency at low power is due to the cold gas thrust. At low power, and thus low ion fraction, the exhaust is primarily neutral propellant and the near-field Hall parameter due to electron-neutral collisions is high ($\Omega \gg 200$). This results in the throat of the nozzle being pushed downstream into the expected plume region and an increase in the effective length of the source region, resulting in a reduced ion Mach number at the detachment location due to the reduction in the nozzle

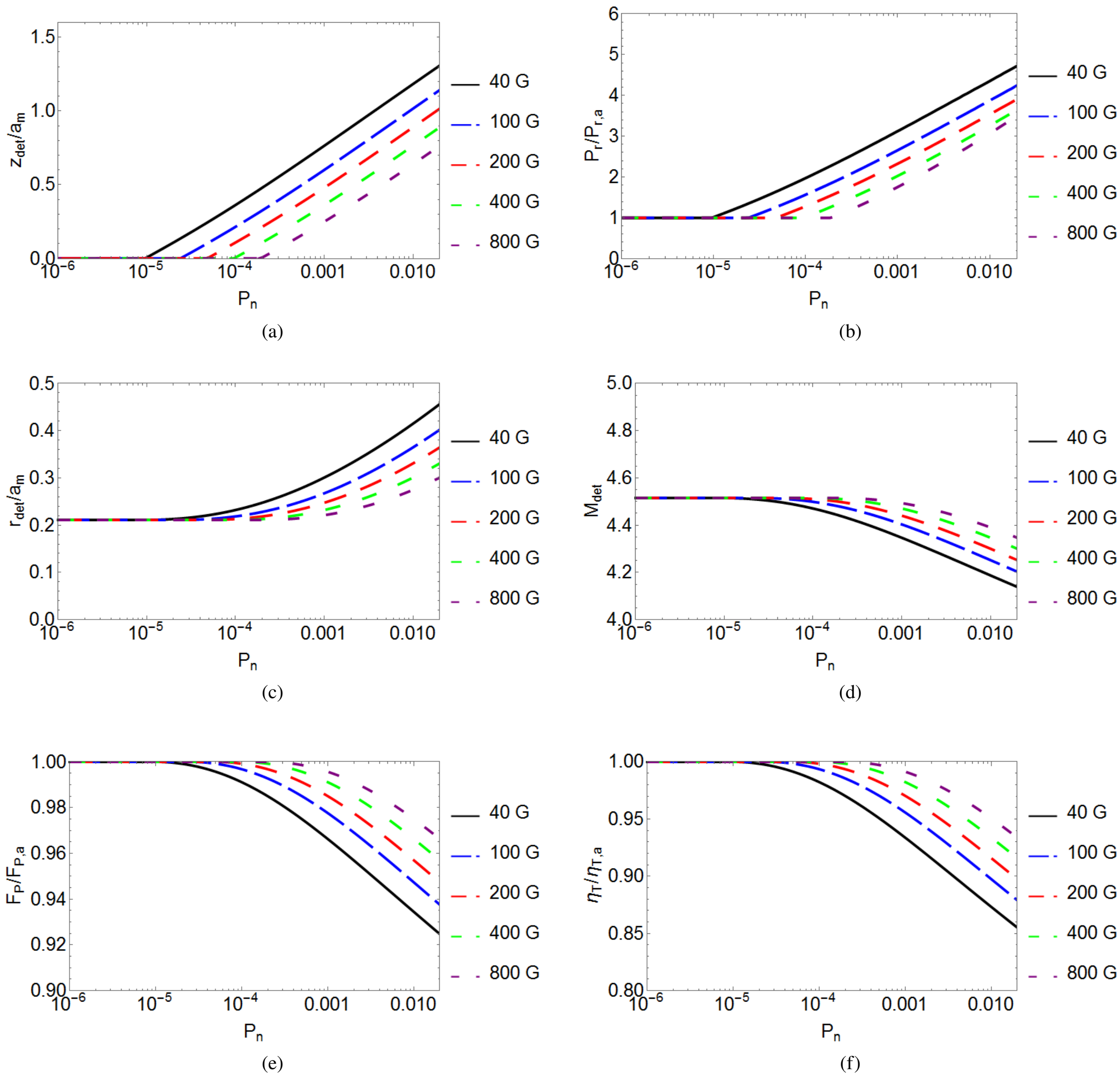

Fig. 12 The near-field neutral pressure dependence of (a) the axial detachment location of the magnetic nozzle, (b) the radial power losses compared to a perfectly attached nozzle, (c) the radial detachment location of the magnetic nozzle, (d) the ion Mach number at the detachment location, (e) the nozzle expansion thrust compared to the nozzle expansion thrust if perfectly attached, and (d) the total efficiency compared to the efficiency if perfectly attached. The model used the MDX magnet, modeled as a single current loop, and source tube configuration. Note that in all cases the plasma density is assumed to be constant ($n_0 \sim 2\times 10^{17}$ m^{-3}), regardless of inflow neutral pressure, and the Lafleur [1] density profile shape is used.

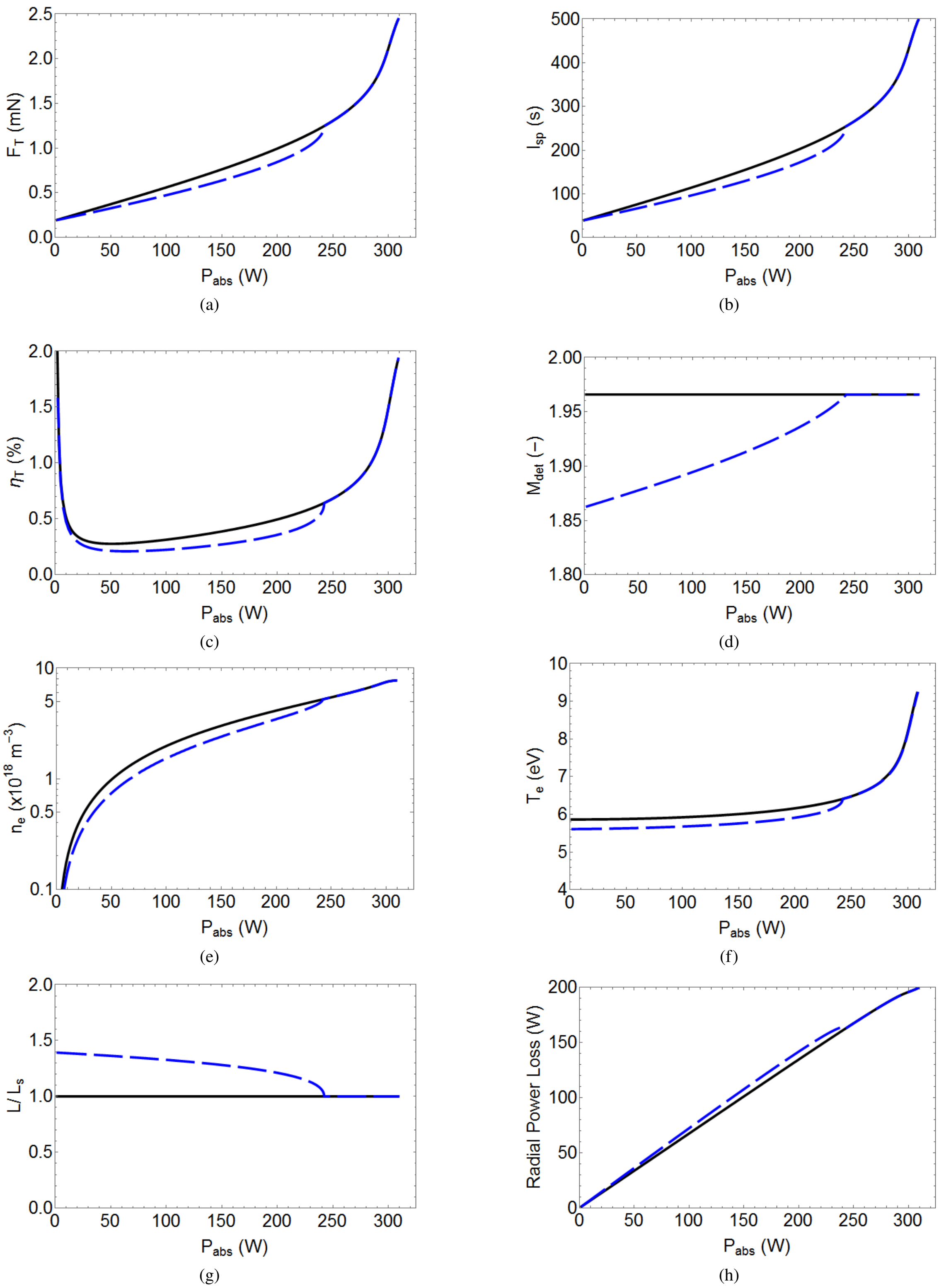

Fig. 13 The impact of near-field resistive detachment on the (a) thrust, (b) specific impulse, (c) total efficiency, (d) ion Mach number at the detachment location, (e) plasma density, (f) electron temperature, (g) effective length of the source region, and (h) the power lost to the walls of the source. The solid curve corresponds to the idealized, fully attached case while the dashed curve includes the non-ideal upstream pressure effects. The MDX physical dimensions are used, but the throat strength is set to 800 G and the propellant flow rate is 0.5 mg/s of xenon. Under these conditions the ion Larmor radius is smaller than the source tube radius, so we use the original Lafleur [1] detachment criterion - where $r_{Li} = r_s$.

area ratio. This is accompanied by a reduced electron temperature, resulting in a reduced plasma density, and enhanced radial power losses to the effective source tube walls.

At intermediate input power ($25 \leq P_{abs} \leq 225$ W) the ion fraction and Hall parameter within the plume increases, but the same trends hold. At $P_{abs} \sim 250$ W the plasma density increases to the point that the Hall parameter reaches the critical threshold ($\Omega \sim 200$) and the plasma begins to be attached throughout the expanding nozzle region, and the model starts to match the idealized, fully attached performance predictions. At this input power level the ion fraction is high enough that the electron temperature also begins to increase, resulting in rapid gains in the thrust, specific impulse, and total efficiency. At $P_{abs} \sim 310$ W the plasma becomes nearly fully ionized and the gains in performance become largely due to an increase in electron temperature via Eq. 27. However, due to the isothermal assumption within the nozzle region [1] these metrics are not bounded except by the electron temperature limits of the chosen power deposition mechanism - for ICP and helicon sources $T_e \leq 10$ eV [2, 4, 5, 16, 28] and for low power electron cyclotron sources $T_e < 30$ eV [29].

C. Impact of Background Pressure on Performance

The effect of background pressure on thrust performance can be modeled by using the same critical Hall parameter threshold of $\Omega = 200$. As illustrated by the results in Figure 14 the primary impact of the neutral background pressure is a shortening of the magnetic nozzle. In Figure 14(a) the length of the nozzle is the distance between the exit plane and the turning point at low background pressures, but sharply diminishes with increasing pressure. At high pressures the magnetic nozzle does not confine the plasma and the discharge becomes equivalent to warm gas expansion. At higher magnetic nozzle strengths the plasma remains attached to the magnetic nozzle at slightly higher background pressures. This shortening of the magnetic nozzle leads to a reduction in the cross-sectional area at the detachment location, which results in the reduced acceleration shown in Figure 14(b). As shown in Figure 14(c) this nozzle shortening also results in a reduction in the total thrust generated by the plasma expansion through the nozzle and the corresponding total efficiency, as illustrated by Figure 14(d). Note that the performance values are relative to the performance of a fully attached magnetic nozzle expanding into a perfect vacuum, and the asymptotes in these figures are due to the MDX source tube diameter and the single current loop electromagnet model.

Like the impact of the near-field neutral pressure the background pressure reduces the thrust and efficiency of the nozzle with increasing pressure by shortening the length of the nozzle, therby limiting the expansion and final ion velocity. In the presence of a sufficiently high background pressure, possibly due to inadequate pumping speed in ground testing facilities, the nozzle effectively disappears and the plasma thermal energy is not efficiently converted into directed kinetic energy. The onset of this background pressure effect can be mitigated at high magnetic nozzle strengths, however this may partially explain the performance reduction of ECRs with increasing facility background pressure [20].

D. Viability of the Solenoidal Antenna Architecture for Efficient Thrust Production

As demonstrated in the divergence efficiency section above the ring discharge structure, with an off-axis density peak, does not significantly impact efficiency performance compared to a center-peaked profile, but does severely enhance power losses to the radial walls. The MEICP work of Kinder and Kushner [25] suggests that a solenoidal antenna architecture, which has heritage in the propulsive magnetic nozzle literature [16], is conducive to the generation of ring discharge structures. In order to avoid the ring discharge structure thrusters utilizing a solenoidal architecture must reduce the strength of the magnetic nozzle which will result in higher radial losses within the source tube via poor plasma confinement within the source region. If the throat magnetic field strength is increased to 100s of Gauss then the zone of maximum power deposition is confined to the edges of the nozzle leading to enhanced edge plasma density, which also causes excessive radial losses.

Interestingly, a secondary effect occurs within the source tube if the magnetic nozzle strength is above the critical threshold for the formation of the ring structure: the power deposition region is off-axis, resulting in a more weakly ionized center core. In cases where power coupling from the antenna is poor this can be compounded by the small power deposition in the core, yielding a high un-ionized neutral population within the thruster exhaust. This un-ionized neutral density near the exit plane of the thruster may result in near-field resistive detachment, further reducing the thrust performance of the device by enhancing radial power losses and by driving the effective nozzle throat downstream. Overall, a design trade exists between a nozzle of sufficient strength to limit radial wall losses within the source tube through plasma confinement and conditions conducive to creating a ring discharge. This compounding of effects detrimental to thrust performance may indicate that solenoidal antenna architectures are unsuitable for efficient thrust production in propulsive magnetic nozzles.

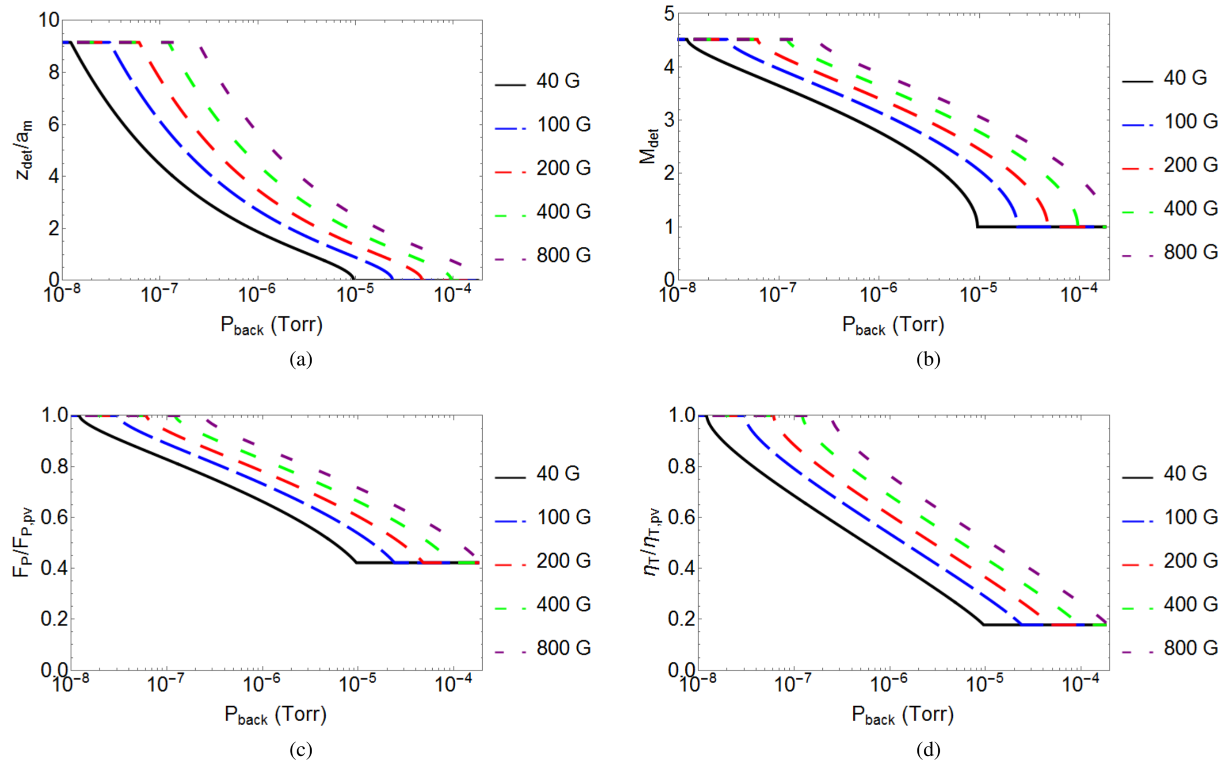

Fig. 14 The background pressure dependence of (a) the axial detachment location of the magnetic nozzle, (b) the ion Mach number at the detachment location, (c) the nozzle expansion thrust compared to the nozzle expansion thrust if exhausting into a perfect vacuum, and (d) the total efficiency compared to the efficiency if exhausting into a perfect vacuum. The model used the MDX magnet, modeled as a single current loop, and source tube configuration.

VII. Conclusion

The quasi-1D model developed by Lafleur [1] and modified by Collard et. al. [18] to handle small magnetic nozzle thrusters where the ions are partially magnetized is adapted to provide information about the impact of plasma density profile shape on the divergence efficiency. This additional efficiency information is obtained through a coordinate frame transfer from cylindrical (r, z) to magnetic (ψ, ξ) coordinates for the plume expansion region.

The density profiles of the MDX measured using a planar double Langmuir probe exhibit an off-axis peak at magnetic fields exceeding $\sim$ 100 G when the experiment incorporated a multi-turn solenoidal antenna. This density profile shape is consistent with ring discharge structures [25], where the region of maximum power deposition is confined near the walls above a critical magnetic field. When the MDX was operated at a throat magnetic field strength of 390 G a large density dip on centerline was observed; when this profile is used to initialize the adapted divergence efficiency model the result was an $\sim$ 2% reduction in the divergence efficiency compared to the center-peaked density profile used in the original Lafleur model [1]. This mild reduction of efficiency performance is due to the confinement of high density in the highly divergent edges of the magnetic nozzle, resulting in larger radial velocity components at the far-field detachment location. The small reduction suggests that the divergence efficiency is relatively insensitive to plasma density profile within the operating envelope of the MDX.

The enhanced edge plasma densities associated with ring discharge structures results in enhanced power losses to the radial walls within the source tube; in the measured 390 G MDX operating case the radial losses were a factor of $\sim$ 1.7 times the losses in the weaker, and less ring discharge-like, magnetic nozzle cases. At constant input power the enhanced radial wall losses reduce the fraction of the total power contributing to thrust production.

The effects of neutral pressure on magnetic nozzle performance is included through the incorporation of the Hall parameter into the quasi-1D model. The critical Hall parameter of $\Omega \sim 200$ is informed by experimental measurements of the MDX at constant power and propellant flow rate and varying magnetic nozzle strength, including neutral pressure measurements using a Stabil ion gauge, magnetic field measurements using a 3-axis Gaussmeter, and ion velocity vectors using 2D time-averaged LIF.

When the model included the effects of high un-ionized neutral density originating from the thruster near-field detachment can be observed. In terms of performance, if near-field pressure is high then the effective source region is extended into the diverging nozzle section, resulting in enhanced radial power losses due to high cross-field transport, and the effective nozzle throat is shifted downstream. The downstream shift of the nozzle throat results in a smaller area ratio between the throat and the far-field detachment location, resulting in a smaller thrust contribution due to plasma expanding through the remainder of the nozzle.

When the model included the effect of background pressure a shortening of the magnetic nozzle is observed. This is due to premature collisional detachment occurring upstream of the nozzle turning point due to the presence of an elevated background neutral population, possibly caused by insufficient pumping in ground test facilities. The shortening of the nozzle also reduces the area expansion ratio of the nozzle, thereby reducing the thrust and efficiency of the system.

In magnetic nozzle thrusters employing a solenoidal antenna architecture a critical magnetic field threshold exists. Below this threshold the magnetic field may not be able to sufficiently confine the plasma in the source tube, thereby resulting in unacceptable radial wall power losses. Above the magnetic field threshold the operating conditions are conducive to creating a ring discharge structure that is characterized by the presence of an off-axis density peak. If this plasma structure is present the thruster will suffer from a slight reduction in divergence efficiency performance, enhanced radial power losses due to elevated edge plasma densities, and may exhibit near-field detachment if the core within the source tube remains un-ionized, possibly further reducing the total thrust generated and the device efficiency. This suggests that a solenoidal antenna architecture may not be suitable for efficiently generating thrust in propulsive magnetic nozzles, but direct performance measurements are required to validate the model results.

Appendix

For completeness, the important intermediate parts of the original quasi-1D model [1] that are not modified by the inclusion of pressure effects are included in this Appendix.

In the source region of the model Lafleur [1] combines the continuity and momentum equations to determine the electron temperature that balances ionization and losses to the walls and into the nozzle. In order to preserve information about radial variations within the source region while reducing the problem to a single dimension a self-similar density profile of the form

$$f(\rho) = \left[1 - (1 - h_R^{1/t})\rho^s\right]^t, \tag{19}$$

where $\rho = r/R_s$ and h_R is the sheath edge-to-center density ratio, is assumed. Based on fits to experimental data the parameters are $t = 6$ and $s = 2$. This includes the radial variations by using an average density determined from $\langle nf \rangle = \beta n$, where β is defined as the radially-averaged density coefficient, or

$$\beta = 2\int_0^1 f(\rho)\rho d\rho = 2\int_0^1 \left[1 - (1 - h_R^{1/t})\rho^s\right]^t \rho d\rho. \tag{20}$$

If the assumptions of small plasma momentum losses to the wall and a collisionless plasma within the source region hold, and the region has a constant cross sectional area the momentum balance is

$$-2 - \xi ln\left(\frac{1-\xi}{1+\xi}\right) + 2\sqrt{1-\xi^2}\left[\tan^{-1}\left(\frac{1-\xi}{\sqrt{1-\xi^2}}\right) - \tan^{-1}\left(\frac{-1-\xi}{\sqrt{1-\xi^2}}\right)\right] = \gamma, \tag{21}$$

with the various grouped terms defined as

$$\gamma = a\frac{K_{iz}}{u_B} - b, \tag{22}$$

$$\xi = \frac{1}{1 - \frac{u_B}{K_{iz}}\frac{b}{a}}, \tag{23}$$

$$a = \frac{\Gamma_0 L_s}{v_g}, \tag{24}$$

and

$$b = \frac{2h_R L_s}{\beta R_s}, \tag{25}$$

where T_e is the electron temperature, Γ_0 is the particle number flux, L_s is the length of the source tube, R_s is the source tube radius, v_g is the neutral particle velocity, and η_m is the mass utilization efficiency. Note that the Bohm speed, $u_B(T_e)$, and the ionization rate, $K_{iz}(T_e)$, are functions of electron temperature while the particle flux, $\Gamma_0(\eta_m)$, is a function of the mass utilization efficiency. Therefore, the momentum balance is a function of the thruster geometry and operating conditions. In the model, Eq. 21 is iteratively solved by incrementing η_m to determine the equilibrium electron temperature that balances ionization and losses to the boundaries of the source region, including losses to the walls and the momentum that enters the diverging nozzle section.

In the nozzle section Eq. 6 can be manipulated into a form that yields the thrust due to the expansion through the nozzle via integrating over the cross sectional area at the detachment point:

$$F_P = \left(\frac{M_{det}^2 + 1}{2M_{det}}\right) F_0 \tag{26}$$

where M_{det} is the ion Mach number at the detachment location and F_0 can be interpreted as the thrust on the back wall;

$$F_0 = q\beta n_0 T_e A_0. \tag{27}$$

In this expression βn_0 is the average plasma density at the throat and A_0 is the cross sectional area of the throat.

A similar manipulation of the neutral gas momentum and continuity equations yields an expression for the cold gas thrust of the neutrals that do not get ionized:

$$F_g = \dot{m} v_g \left(1 + \frac{qT_g}{m_i v_g^2}\right), \tag{28}$$

and the total thrust can be found as the sum of Eqs. 26 and 28, or $F_T = F_P + F_g$. In this equation $\dot{m}$ is the propellant mass flow rate, m_i is the ion mass, and T_g is the neutral gas temperature.

Functionally, the non-ideal resistive pressure effects are included by solving for the equilibrium electron temperature using Eq. 21 as if the pressure effects are negligible and then calculating the plasma density, Hall parameter throughout the plume, and the near-field detachment location. The effective length of the source region is updated, influencing Eqs. 24 and 25, and this process is iterated until the electron temperature converges.

Acknowledgments

This material is based upon work supported by the National Science Foundation Graduate Research Fellowship Program under Grant No. DGE 1256260. Thank you to the members of the Plasmadynamics and Electric Propulsion Laboratory for their insightful discussion concerning this research.

References

[1] Lafleur, T., "Helicon plasma thruster discharge model," *Physics of Plasmas*, Vol. 21, No. 4, 2014, p. 043507.

[2] Takahashi, K., Lafleur, T., Charles, C., Alexander, P., Boswell, R., Perren, M., Laine, R., Pottinger, S., Lappas, V., and Harle, T., "Direct thrust measurement of a permanent magnet helicon double layer thruster," *Applied Physics Letters*, Vol. 98, No. 14, 2011, p. 141503.

[3] Takahashi, K., Charles, C., Boswell, R., and Ando, A., "Performance improvement of a permanent magnet helicon plasma thruster," *Journal of Physics D: Applied Physics*, Vol. 46, No. 35, 2013, p. 352001.

[4] Charles, C., and Boswell, R., "Laboratory evidence of a supersonic ion beam generated by a current-free "helicon" double-layer," *Physics of Plasmas (1994-present)*, Vol. 11, No. 4, 2004, pp. 1706–1714.

[5] Charles, C., and Boswell, R., "Current-free double-layer formation in a high-density helicon discharge," *Applied Physics Letters*, Vol. 82, 2003, p. 1356.

[6] Williams, L. T., and Walker, M. L., "Thrust Measurements of a Helicon Plasma Source," *AIAA/ASME/SAE/ASEE Joint Propulsion Conference & Exhibit*, 2011.

[7] Williams, L. T., and Walker, M. L., "Thrust measurements of a radio frequency plasma source," *Journal of Propulsion and Power*, Vol. 29, No. 3, 2013, pp. 520–527.

[8] Little, J. M., "Performance Scaling of Magnetic Nozzles for Electric Propulsion," Ph.D. thesis, 2015.

[9] Merino, M., and Ahedo, E., "Plasma detachment in a propulsive magnetic nozzle via ion demagnetization," *Plasma Sources Science and Technology*, Vol. 23, No. 3, 2014, p. 032001.

[10] Fruchtman, A., Takahashi, K., Charles, C., and Boswell, R., "A magnetic nozzle calculation of the force on a plasma," *Physics of Plasmas (1994-present)*, Vol. 19, No. 3, 2012, p. 033507.

[11] Ahedo, E., and Merino, M., "On plasma detachment in propulsive magnetic nozzles," *Physics of Plasmas (1994-present)*, Vol. 18, No. 5, 2011, p. 053504.

[12] Sheehan, J. P., Collard, T. A., Longmier, B. W., and Reese, I., *New Low-Power Plasma Thruster for Nanosatellites*, Propulsion and Energy Forum, American Institute of Aeronautics and Astronautics, 2014. Doi:10.2514/6.2014-3914.

[13] Sheehan, J., Collard, T. A., Ostermann, M. E., Dale, E. T., Wachs, B. N., and Longmier, B. W., "Initial operation of the CubeSat Ambipolar Thruster," *Plasma Sciences (ICOPS), 2015 IEEE International Conference on*, IEEE, 2015, pp. 1–1.

[14] Collard, T., and Sheehan, J. P., *Preliminary Measurements of an Integrated Prototype of the CubeSat Ambipolar Thruster*, AIAA Propulsion and Energy Forum, American Institute of Aeronautics and Astronautics, 2016. Doi:10.2514/6.2016-5042.

[15] Longmier, B. W., Squire, J. P., Cassady, L. D., Ballenger, M. G., Carter, M. D., Olsen, C., Ilin, A. V., Glover, T. W., McCaskill, G. E., and Dıaz, F. C., "VASIMR VX-200 performance measurements and helicon throttle tables using argon and krypton," *32nd International Electric Propulsion Conference*, 2011.

[16] Takahashi, K., Akahoshi, H., Charles, C., Boswell, R. W., and Ando, A., "High temperature electrons exhausted from rf plasma sources along a magnetic nozzle," *Physics of Plasmas*, Vol. 24, No. 8, 2017, p. 084503.

[17] Hall, S. J., Cusson, S. E., and Gallimore, A. D., "30-kW Performance of a 100-kW Class Nested-Channel Hall Thruster," *34th International Electric Propulsion Conference, Hyogo-Kobe, Japan*, 2015.

[18] Collard, T. A., Sheehan, J. P., and Jorns, B. A., "A Numerical Examination of the Performance of Small Magnetic Nozzle Thrusters," 2017. Doi:10.2514/6.2017-4721.

[19] Collard, T. A., Byrne, M. P., Hepner, S. T., Durot, C. J., and Jorns, B. A., "Investigation of Detachment in a Miniature Magnetic Nozzle Source," 2017.

[20] Vialis, T., Jarrige, J., and Packan, D., "Geometry optimization and effect of gas propellant in an electron cyclotron resonance plasma thruster," 2017.

[21] Merino, M., and Ahedo, E., "Plasma detachment mechanisms in a magnetic nozzle," *AIAA Paper*, , No. 2011-5999, 2011.

[22] Simpson, J. C., Lane, J. E., Immer, C. D., and Youngquist, R. C., "Simple analytic expressions for the magnetic field of a circular current loop," 2001.

[23] Durot, C. J., Gallimore, A. D., and Smith, T. B., "Validation and evaluation of a novel time-resolved laser-induced fluorescence technique," *Review of Scientific Instruments*, Vol. 85, No. 1, 2014, p. 013508.

[24] Saloman, E. B., "Energy Levels and Observed Spectral Lines of Xenon, XeI through XeLIV," *Journal of Physical and Chemical Reference Data*, Vol. 33, No. 3, 2004, pp. 765–921.

[25] Kinder, R. L., and Kushner, M. J., "Wave propagation and power deposition in magnetically enhanced inductively coupled and helicon plasma sources," *Journal of Vacuum Science & Technology A: Vacuum, Surfaces, and Films*, Vol. 19, No. 1, 2001, pp. 76–86.

[26] Kinder, R. L., and Kushner, M. J., "Noncollisional heating and electron energy distributions in magnetically enhanced inductively coupled and helicon plasma sources," *Journal of Applied Physics*, Vol. 90, No. 8, 2001, pp. 3699–3712.

[27] Eckert, H. U., "Diffusion Theory of the Electrodeless Ring Discharge," *Journal of Applied Physics*, Vol. 33, No. 9, 1962, pp. 2780–2788.

[28] Boswell, R., "Very efficient plasma generation by whistler waves near the lower hybrid frequency," *Plasma Physics and Controlled Fusion*, Vol. 26, No. 10, 1984, p. 1147.

[29] Lafleur, T., Cannat, F., Jarrige, J., Elias, P., and Packan, D., "Electron dynamics and ion acceleration in expanding-plasma thrusters," *Plasma Sources Science and Technology*, Vol. 24, No. 6, 2015, p. 065013.